

# Microstructure, Mechanical and Corrosion Properties of Friction Stir-Processed AISI D2 Tool Steel

Noushin Yasavol and Hassan Jafari

(Submitted August 31, 2014; in revised form February 2, 2015; published online March 24, 2015)

In this study, AISI D2 tool steel underwent friction stir processing (FSP). The microstructure, mechanical properties, and corrosion resistance of the FSPed materials were then evaluated. A flat WC-Co tool was used; the rotation rate of the tool varied from 400 to 800 rpm, and the travel speed was maintained constant at 385 mm/s during the process. FSP improved mechanical properties and produced ultrafine-grained surface layers in the tool steel. Mechanical properties improvement is attributed to the homogenous distribution of two types of fine (0.2–0.3  $\mu\text{m}$ ) and coarse (1.6  $\mu\text{m}$ ) carbides in duplex ferrite-martensite matrix. In addition to the refinement of the carbides, the homogenous dispersion of the particles was found to be more effective in enhancing mechanical properties at 500 rpm tool rotation rate. The improved corrosion resistance was observed and is attributed to the volume fraction of low-angle grain boundaries produced after friction stir process of the AISI D2 steel.

**Keywords** AISI D2 tool steel, corrosion resistance, friction stir processing, nanohardness

## 1. Introduction

Over the two past decades, AISI D2 tool steel, a commercial cold work steel grade, has captivated the interest of several industries and many scientists. Because of its low cost and high performance, AISI D2 steel is used in forming punches, blanking, cold forging and coining dies, spinning tools, and slitting cutters (Ref 1-3). To provide the harder surface and improve the performance, surface of this steel has been reported to coat with TiN or TiAl (Ref 2, 4, 5). Boronizing improves the mechanical strength and corrosion resistance of AISI D2 tool steel, especially at high temperatures (Ref 6). Since boride layers are brittle, it is preferred to use these layers in non-pulse loading applications. Furthermore, deposition of multilayered WC-(Cr<sub>1-x</sub>Al<sub>x</sub>)N coatings, using cathodic arc ion-plating process, includes higher wear resistance, strength, and chemical stability. However, the corrosion performance of the coated steel is affected by small structural defects such as pores, pinholes, and microcracks formed during or after the deposition process (Ref 7). Due to the aforementioned difficulties and limitations of the traditional surface engineering techniques, recent emphasis has been focused on using friction stir processing (FSP) as an alternative approach in surface microstructure refinement of many metals and alloys (Ref 8-11). FSP, as an environmentally friendly efficient process (Ref 12), requires relatively simple and inexpensive mechanical procedures. A non-consumable rotating tool is inserted through the metallic surface that induces frictional heat and plastic defor-

mation at the processing location. Thereby, a solid-state dynamic recrystallization occurs, and the formation of extremely refined surface layers is promoted (Ref 13).

Literature reviewing reveals few publications reporting the implementation of FSP for tool steels. Aldajah et al. (Ref 14) reported the improvement in tribological performance of a high carbon steel using FSP. Chen and Nakata (Ref 15) claimed that using FSP improves tensile and wear properties of the processed area of SKD61 tool steel due to the microstructure refinement and the formation of relatively fine needle martensitic structure. Morisada et al. (Ref 16) characterized microstructure and hardness of a cold work AISI D2 tool steel in combination with laser surface melting and FSP. Although FSP was pointed out as a process refining the microstructure of this steel, the impact of different FSP parameters on the microstructure evolution was not well established. Therefore, the present work aimed at studying the evolution of surface microstructure as well as the mechanical and corrosion properties of AISI D2 tool steel underwent FSP at various rotation rates.

## 2. Experimental Procedure

An as-annealed AISI D2 cold-worked die steel plate of 3-mm thickness with the chemical composition of 11.40Cr-1.49C-0.82Mo-0.79V-0.40Si-0.35Mn-0.31Ni-Bal Fe (in wt.%), as the substrate material, underwent FSP using a columnar WC-Co flat shoulder tool with 16 mm diameter. A schematic illustration of the FSP and rotating tool is shown in Fig. 1. The FSP was accomplished in position control, using 3° tool tilt angle ( $\alpha$ ) and 0.1 mm tool penetration into steel plate. A constant traverse speed of 385 mm/min and four different tool rotation rates of 400, 500, 600, and 800 rpm were used as the processing parameters. Argon gas was used for surface shielding during FSP. The processed workpieces were sectioned transverse to the FSP direction, mechanically polished, and etched with Nital solution. The microstructure of the FSPed zones was examined using optical microscope (OM) and field-emission scanning electron microscope (FESEM, Hitachi

Noushin Yasavol, Department of Materials Engineering, Tarbiat Modares University, 14115-143 Tehran, Iran; and Hassan Jafari, Department of Materials Engineering, Faculty of Mechanical Engineering, Shahid Rajaei Teacher Training University, 16785-136 Tehran, Iran. Contact e-mail: yasavol114@gmail.com.

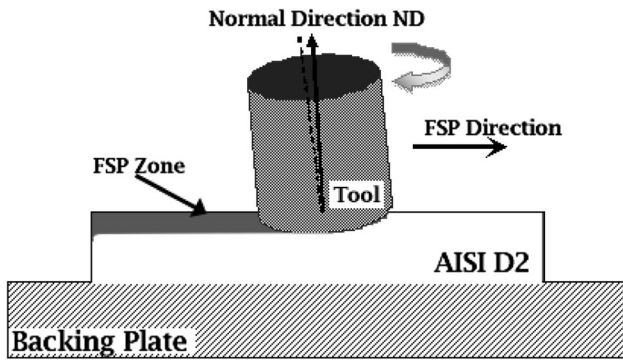


**Fig. 1** Schematic of the FSP setup

S-4300SE) equipped with an electron backscatter diffraction (EBSD) system operated at 15 kV. The obtained EBSD data were characterized by TSL-OIM analysis software Ver. 5.3. The matrix and the carbide structures were identified using micro x-ray diffraction (XRD, X'Pert MPD Philips) with Cu K $\alpha$  1.78897 Å.

Nanohardness and tensile tests were performed to evaluate the mechanical properties of the processed specimens. Hardness of the FSPed samples was measured using Vickers nano-indentations under 30 mN loads in 16  $\times$  4 arrays extending from the stir zones (SZs) into the base metal (BM). The tensile test specimens were cut from the FSPed plates with the tensile axis perpendicular to the FSP traveling direction. Tensile test was carried out in a 10 kN Instron 4206 testing machine operating at room temperature with a 0.5 min<sup>-1</sup> strain rate. Strain data acquisition was performed by digital image correlation (DIC) using Aramis 3D 5 M optical system (GOM GmbH). The processed samples had been prepared by spraying a random black pattern over the previously matt white painted surface of the transverse samples before testing, in order to facilitate strain data acquisition by DIC.

Corrosion behavior of the processed samples was assessed in 3.5 wt.% NaCl solution using an Autolab potentiostat/galvanostat device. Specimens of 1  $\times$  1 cm<sup>2</sup> were cut from the FSPed samples to expose 1 cm<sup>2</sup> to 250 mL of the solution during the experiment. A scan rate of 1 mV/s starting from -150 mV below to 50 mV above testing cell instant potential was operated to run the experiment. A conventional three-electrode cell consisting of a reference electrode (Ag/AgCl saturated in KCl), a counter electrode (a graphite rod), and a working electrode (the specimen) was set to measure the electrochemical parameters of the specimens during corrosion test. The corrosion potential ( $E_{\text{corr}}$ ) and corrosion current density ( $i_{\text{corr}}$ ) of each specimen were determined through Tafel plot method.

### 3. Results and Discussion

#### 3.1 Microstructure Examination

Figure 2 shows the optical micrograph of the as-annealed AISI D2 tool steel. This unprocessed substrate consists of coarse carbide particles with an average size of 2-40  $\mu\text{m}$  within a fine ferrite matrix. In contrast, Fig. 3 illustrates a low-magnification view of the transverse cross-section of the sample

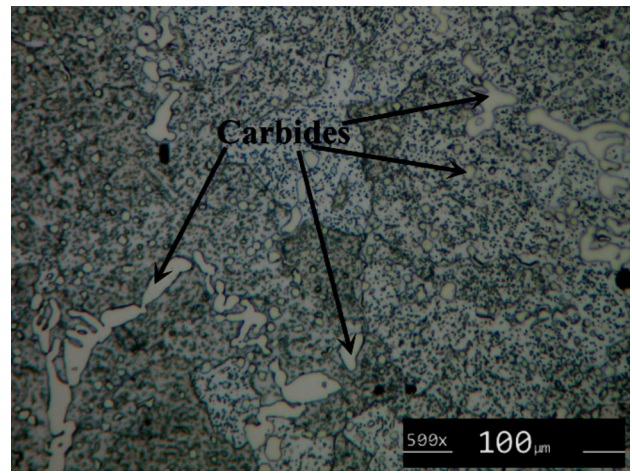


**Fig. 2** Optical microstructure of the as-annealed AISI D2 tool steel

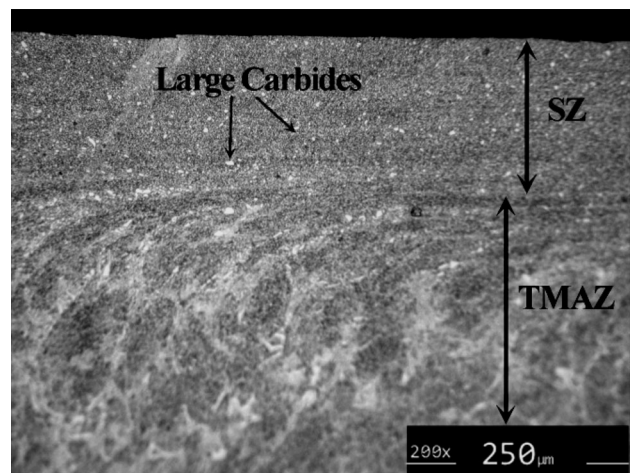


**Fig. 3** Optical micrograph of FSPed sample at tool rotation rate of 400 rpm

processed at the rotation rate of 400 rpm. Two distinct zones can be identified: the SZ, characterized by the refined microstructure, and the thermo-mechanical affected zone (TMAZ) characterized by the plastically deformed grains oriented according to the tool traverse direction. Similar microstructural modification was also seen in the samples processed at the rotation rates of 500, 600, and 800 rpm. It is known that the intensive plastic deformation combined with high temperature caused by FSP results in the formation of a recrystallized and fine microstructure within the SZ-containing fine strengthening particles of carbides (Ref 17).

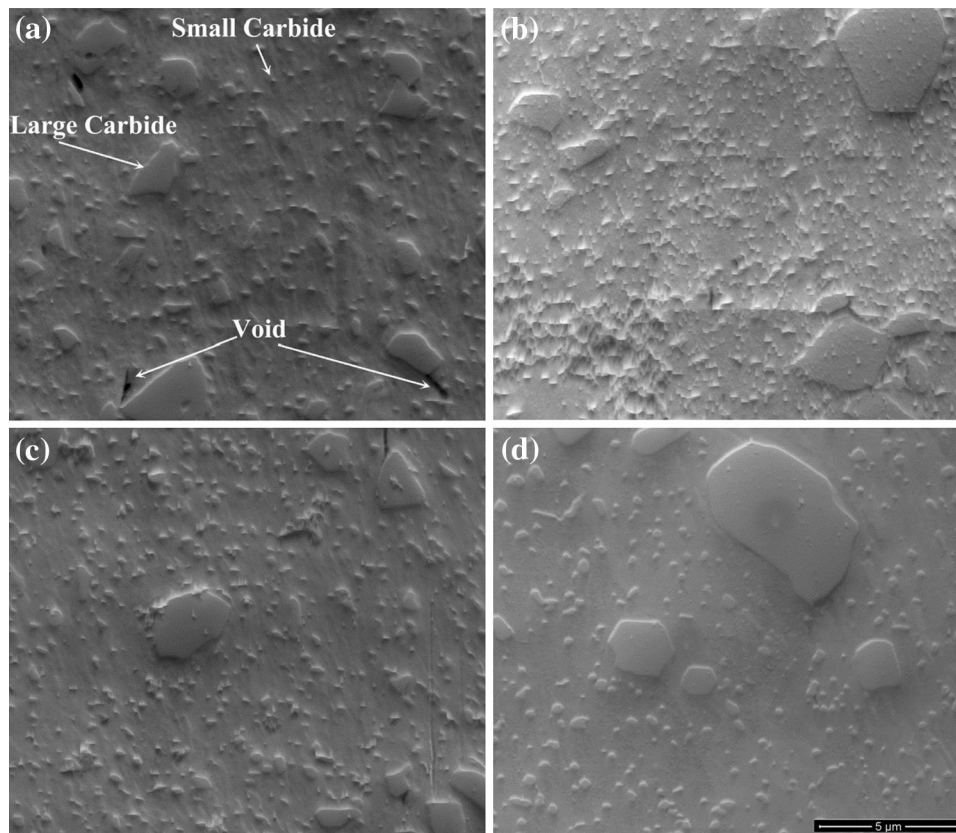
The depth of SZ was measured to be 80  $\mu\text{m}$  at the rotation rate of 400 rpm (Fig. 3). It increased to 100  $\mu\text{m}$  at 500 rpm and decreased significantly to 37 and 20  $\mu\text{m}$  at the rotation rates of 600 and 800 rpm, respectively. The decrease in the FSP depth can be ascribed to the slippage of the tool shoulder. The drop-off of the width and depth of the SZ within the samples indicate that lower heat input introduced into the samples at the higher rotation rates (Ref 18). However, Su et al. (Ref 19) reported that FSP at higher rotation rates leads to faster cooling rates causing more microstructure refinement than those obtained at lower rotation rates.

Figure 4 shows SEM images of SZ of the samples processed at the rotation rates of 400-800 rpm. It can be observed that a large number of small semi-spheroidized particles are homogeneously distributed in the matrix. In addition, a small number of coarse angular/blocky particles are randomly embedded in the matrix. The average size of the former and the latter was measured as 0.2-0.3 and 1.6  $\mu\text{m}$ , respectively, for all processed samples, which are much lower compared to those of the substrate (30  $\mu\text{m}$ ). It can be concluded that FSP results in a significant breakdown of carbides; subsequently it develops a uniform distribution of smaller broken carbides in the matrix. However, it seems that the stirring action and the forging force of the tool were not strong enough to break down or dissolve some large substrate carbides; just grinding their sharp edges. Furthermore, it can be seen that the density and distribution of the carbides in the sample processed at the rotation rate of 500 rpm (Fig. 4b) are different from those of the samples processed at the other rotation rates (Fig. 4a, c, and d), irrespective of the particles size. In fact, the increment of tool rotation rate from 400 to 500 rpm was accompanied with the increase in induced pressure, temperature, and string action of the shoulder leading to homogeneous dense distribution of carbide particles inside the processed matrix. However, this behavior was not observed in the samples processes with the rotation rates increased from 500 to 600 and 800 rpm. Therefore, it brought about less homogeneous dense distribution of the small carbide particles. Similar carbide distribution throughout the ferrite-cementite microstructure was already observed in the previous work on FSWed samples of the SC35 steel (Ref 17).

Another important microstructural feature that can be seen in Fig. 4(a) is the presence of some microvoids/discontinuities located around the large carbides in the SZ of the sample processed at the rotation rate of 400 rpm. Xue et al. (Ref 20) and Zareie Rajani et al. (Ref 21) also observed discontinuities at the interface of aluminum and hard copper clusters that are dragged inside a softer aluminum matrix, during dissimilar FSW of aluminum to copper and aluminum to brass, respectively. It was reported that the sharp geometry of copper clusters makes material filling very difficult promoting the formation of very large discontinuities. Similar difficulties in material flow around the AISI D2 carbide clusters can be referred to the discontinuities observed in Fig. 4(a).

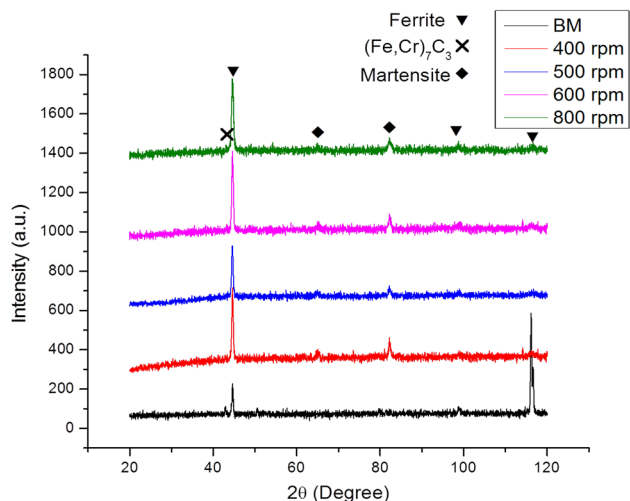
### 3.2 XRD Analysis

Figure 5 shows XRD patterns of the unprocessed and the processed AISI D2 steel samples. The XRD pattern corresponding to the unprocessed sample (BM) reveals the presence of two phases:  $\alpha$ -ferrite ( $\alpha$ -Fe) and  $(\text{Fe, Cr})_7\text{C}_3$  carbide. Figure 5 also reveals a change in the XRD patterns of the processed samples which is the disappearance of the highest ferrite peak at  $2\theta = 116^\circ$ . However, two new peaks emerged at  $2\theta = 64.9^\circ$  and  $2\theta = 82.2^\circ$  for all FSPed samples. This can be attributed to the martensite phase formation (Ref 22). Another phase in the XRD patterns is related to carbide phase in the form of  $(\text{Fe-Cr})_7\text{C}_3$ . However, it is important to note that AISI D2 is a high chrome-carbon tool steel with a large amount of carbides inducing overlapping some characteristic peaks of the carbides with those of the martensite in the patterns (Ref 20).



**Fig. 4** SEM microstructures of FSPed stir zones, at rotation rates of (a) 400, (b) 500, (c) 600, and (d) 800 rpm

Therefore, it can be concluded that FSP transformed the ferrite-carbide structure of the unprocessed sample into a martensite-carbide-ferrite structure. This microstructural evolution in the



**Fig. 5** XRD patterns of substrate and FSPed samples processed at different tool rotation rates (Color figure online)

SZ can be explained by the concurrent occurrence of heating and severe plastic deformation during FSP and subsequent rapid cooling. Although it is generally known that the  $A_1$  and  $A_{cm}$  temperatures of AISI D2 steel are 807 and 850 °C, respectively (Ref 23), the slippage of the tool at the rotation rates of 600 and 800 rpm and the reduction in the depth of SZ indicate that these temperatures could not be easily obtained during FSP. Therefore, the ferrite-carbide structure was sheared plastically during FSP and experienced a solid-state shear transformation to martensite (Ref 24).

## 4. Mechanical Properties

### 4.1 Nanohardness

The effect of FSP on the distribution of mechanical nanoindentation of the AISI D2 cross-section is illustrated in Fig. 6. The SZ of all samples exhibits higher nanohardness values compared to that of the substrate. Similar results were reported by Sato et al. (Ref 25) for 2507 super duplex stainless steel. Figure 6 also illustrates that the nanohardness distribution is very heterogeneous across all the processed surfaces which can be ascribed to the corresponding microstructure shown in

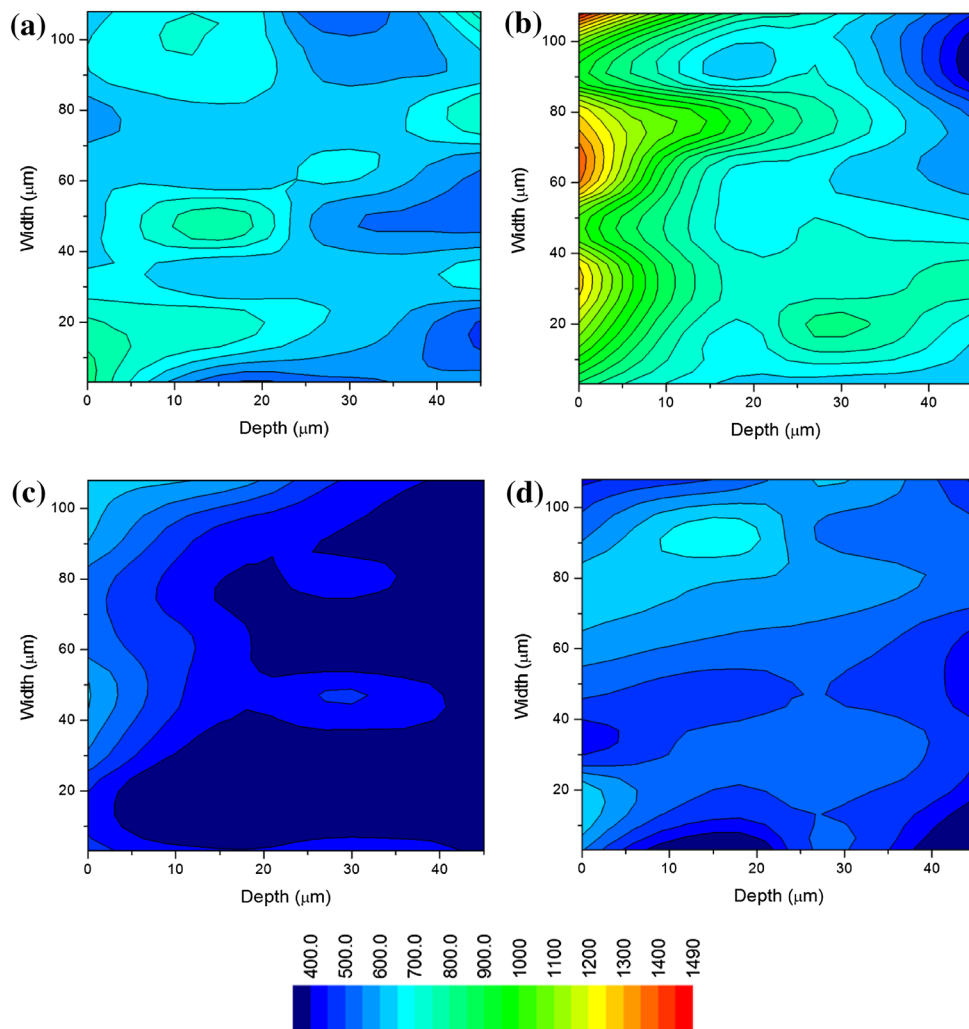


**Fig. 6** Nanohardness distribution of the cross-section of FSPed samples at tool rotation rates of (a) 400, (b) 500, (c) 600, and (d) 800 rpm (Color figure online)

Fig. 4. In addition, the significant differences in nanohardness values and distribution can also be noticed by comparing the nanohardness maps of the samples processed under different conditions. The highest nanohardness value in the SZ was measured as 870 HV (Fig. 6a), while it was found to increase to 1400 HV for the sample processed at the rotation rate of 500 rpm (Fig. 6b). In contrast, the nanohardness value of the samples processed at the rotation rates of 600 and 800 rpm did not exceed 640 and 750 HV, respectively (Fig. 6c and d). Furthermore, the localized high hardness regions can be seen in the nanohardness map of the samples FSPed at the rotation rates of 600 and 800 rpm, which was accompanied with discontinuous SZ denoting tool slippage during the process.

It is well known that such hardness distributions reported in Fig. 6 may result by the concurrent effect of three strengthening mechanisms (Ref 26), precipitation, grain size, and solid-solution strengthening. According to the micrographs given in Fig. 3 and 4, it can be concluded that in the SZ of all samples, the carbide particles size was significantly reduced to 0.2-0.3 and 1.6  $\mu\text{m}$  for small and coarse carbide particles, respectively. Therefore, increasing the nanohardness value should be related to the dense distribution of very small strengthening particles (Ref 27) in fine-grained matrix of the SZ originating from the dynamic recrystallization (Ref 28). Moreover, the martensitic phase formation, as mentioned earlier, may contribute to the hardness improvement. All these could be responsible for the non-uniform nanohardness distributions, as well as for the significant differences in the nanohardness values among samples. Furthermore, it can be seen (Fig. 4) that apart from carbides refinement, carbide distribution also varies within the SZ of the samples underwent FSP using different rotation rates. Increasing the rotation rate from 400 to 500 rpm uniformly increased dense dispersion of the carbide particles in the ferrite matrix. This may be attributed to the higher temperature and more stirring action associated with the higher tool rotation rate (Ref 29, 30). In contrast, increasing the rotation rate to 600 and 800 rpm brought about either a decrease in the SZ depth or a reduction in heat input of FSPed samples, leading to low dense of the small carbide particles. Therefore, it seems that using rotation rate of 500 rpm refined highly dense small strengthening particles distributed in the matrix resulting in the formation of modified surface layer with the highest nanohardness value.

#### 4.2 Tensile Strength

In order to assess the influence of the extent of the continuities on surface strength, some tensile tests were performed using transverse FSPed specimens. Since the substrate as a softer part of the tensile sample was 2 mm thick and the hard FSPed surface was 30  $\mu\text{m}$  depth, it is expectable that the deformation of the softer substrate induces thin localisation failure in the substrate discontinuities locations under tensile loading. In these locations, cracks and/or voids are responsible for such a localized failure. Figure 7 shows the results of tensile tests, strain maps, and strain distribution of all samples. Considering the results given in Fig. 7, it can be inferred that the deformation registered for very thin processed surface is always lower than that of registered in the substrate in all FSPed samples. It is also important to note that no significant variations in strain values or surface damage were captured by the optical system inside the SZ area. This indicates

that the distribution and strength of the structural discontinuities/imperfections of the processed surfaces have no noteworthy effect on surface strength (Ref 31).

#### 4.3 Corrosion Properties

The potentiodynamic curves shown in Fig. 8 indicate that the corrosion behavior of all the FSPed samples is almost similar with that of the unprocessed sample. The electrochemical parameters ( $E_{\text{corr}}$  and  $i_{\text{corr}}$ ) were extracted from the curves and reported in Table 1. It can be found that the FSP at the rotation rates of 400, 500 and 600 rpm lowers the corrosion current densities ( $i_{\text{corr}}$ ) of the samples, compared to the unprocessed and 800 rpm FSPed samples. In addition, the

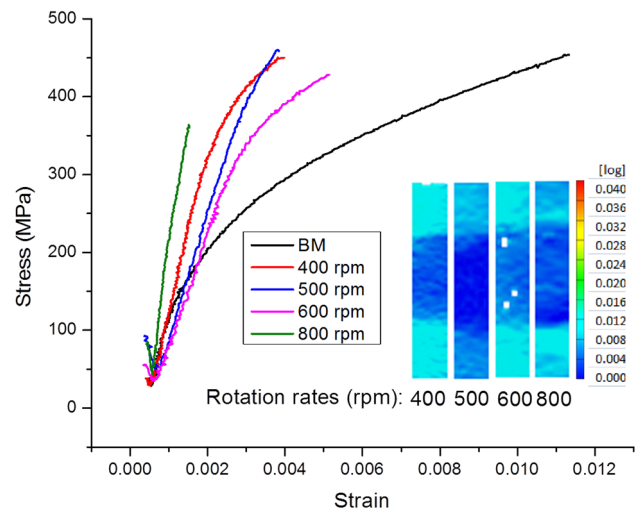


Fig. 7 Strain maps of the base material and FSPed samples at different tool rotation rates (Color figure online)

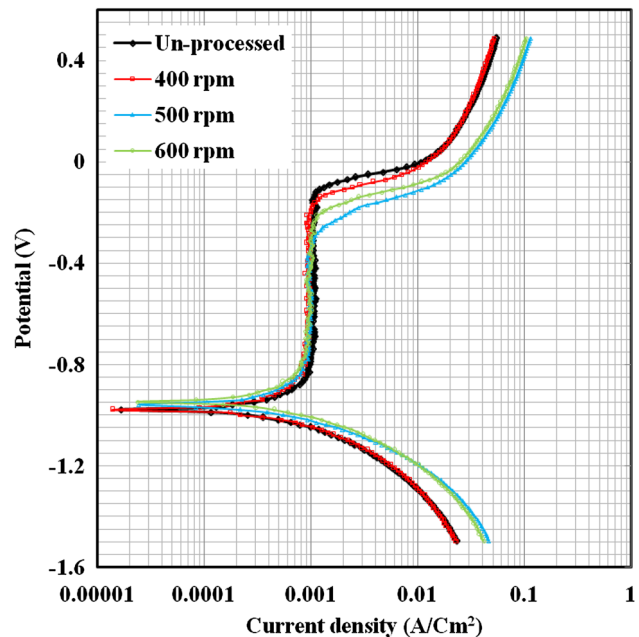


Fig. 8 The potentiodynamic polarization curves of the unprocessed and FSPed specimens in 3.5 wt.% NaCl solution (Scan rate = 1 mV/s) (Color figure online)

**Table 1 Corrosion parameters of FSPed AISI D2 at different rotation rates**

FSP rotation rates, rpm	Potential, V	Current density, A/cm <sup>2</sup>
Unprocessed	-1.02	$1.05 \times 10^{-3}$
400	-1	$9.73 \times 10^{-4}$
500	-1.02	$9.95 \times 10^{-4}$
600	-0.95	$9.93 \times 10^{-4}$
800	-0.92	$1.04 \times 10^{-3}$

**Table 2 Grain boundary fraction of FSPed AISI D2 at different rotation rates**

Rotation rate, rpm	Grain boundary fraction (2°-15°)	Grain boundary fraction (15°-180°)
400	0.189	0.811
500	0.241	0.759
600	0.220	0.780
800	0.376	0.624

processed samples show nearly the same corrosion potential. It should be noted that the potentials obtained for the FSPed samples are very close to that of TiN thin films deposited on AISI D2 reported by Jia-Hong et al. (Ref 32), while the corrosion current densities of the FSPed samples are much higher than that of the WC-(Cr<sub>1-x</sub>Al<sub>x</sub>)N-coated AISI D2 reported by Lee et al. (Ref 7).

Comparing the potentiodynamic polarization curves shown in Fig. 8 with the depth of the SZ of the processed samples, it can be inferred that the processing depth of all FSPed samples does not influence their corrosion behavior. As previously mentioned, an increase in FSP rotation rates reduced the processed depth, while the corrosion behavior of FSPed samples did not change accordingly. This is in disagreement with the results reported by Jia-Hong et al. (Ref 32), the corrosion areas decreased by increasing the thickness of film in AISI D2-coated samples at different thicknesses of TiN layers. In addition, the distribution of carbide particles and grain refinement achieved using different FSP rotation rates, also, are not in line with the corrosion behavior. Moreover, according to the XRD results (Fig. 5), the microstructure changes, from ferrite-carbide to ferrite-martensite-carbide, that occurred due to the FSP do not explain the corrosion behavior. This can be referred to the martensite phase appearance with low corrosion resistance compared with that of the ferrite phase appearance. Furthermore, the microstructure alterations in FSPed samples were not very distinct. Therefore, the trend variations of the corrosion behavior of FSPed samples should be affected by the other parameters. According to FSP, dynamic recovery and dynamic recrystallization are the characteristic phenomena of the FSP/W which severely depend on the processing parameters. Table 2 reports grain boundary fraction of FSPed samples at different rotation rates. It can be observed that an increase in the rotation rate influences the grain boundary fraction of the SZs. The highest low-angle grain boundary fraction (with high energy) compared to high-angle grain boundary (with low energy) relates to the FSPed sample at the rotation rates of 500 rpm. While the samples processed at the rotation rates of 400, 600 and 800 rpm contain lower grain

boundary fractions with low angle grain boundaries, which provide higher corrosion resistance. In fact, the high energy low-angle grain boundaries are sustainable to corrosion. In contrast, the low-energy high-angle grain boundaries are resistant to corrosive solution. Therefore, the corrosion resistance of FSPed samples followed the grain boundaries fractions formed during dynamic recrystallization of FSP.

## 5. Conclusion

In this study, AISI D2 tool steel underwent FSP at various rotation rates of 400-800 rpm. It was observed that the microstructure of all the stir zones consists of the homogeneously distributed fine carbides throughout the matrix of ferrite and martensite. The nanohardness measurements showed two to four times increment in the processed surface hardness for the 400 and 500 rpm samples in comparison with that of the substrate. The decrease in the tool pressure to the FSPed samples caused low dense distribution of the small carbide particles within the processed surfaces and lowered the nanohardness value of the samples at the higher rotation rates of 600 and 800 rpm compared to that of the 500 rpm rotation rate. The extremely hard and thin processed surfaces were observed to be deformed less than the substrate under tensile loading. Surface mechanical properties of AISI D2 were improved due to the uniform dispersion of the fine carbide particles and martensitic transformation. The corrosion resistance of FSPed samples increased compared to that of the unprocessed sample. The improved corrosion behavior was attributed to the higher fraction of the low-angle grain boundaries obtained by FSP.

## References

1. C. Surberg, P. Stratton, and K. Lingenhole, The Effect of Some Heat Treatment Parameters on the Dimensional Stability of AISI, D2, *Cryogenics*, 2008, **48**(1-2), p 42-47
2. M.H. Staia, Y. Pérez-Delgado, C. Sanchez, A. Castro, E. Le Bourhis, and E.S. Puchi-Cabrera, Hardness Properties and High-Temperature Wear Behavior of Nitrided AISI, D2 Tool Steel, Prior and After PAPVD Coating, *Wear*, 2009, **267**(9-10), p 1452-1461
3. W.L. Pan, G.P. Yu, and J.H. Huang, Mechanical Properties of Ion-Plated TiN Films on AISI, D2 Steel, *Surf. Coat. Technol.*, 1998, **110**, p 111-119
4. Y. Guu, AFM Surface Imaging of AISI, D2 Tool Steel Machined by the EDM Process, *Appl. Surf. Sci.*, 2005, **242**(3-4), p 245-250
5. C.K.N. Oliveira, C.L. Benassi, and L.C. Casteletti, Evaluation of Hard Coatings Obtained on AISI, D2 Steel by Thermo-reactive Deposition Treatment, *Surf. Coat. Technol.*, 2006, **201**, p 1880-1885
6. E. Atk, U. Yunker, and C. Meri, The Effects of Conventional Heat Treatment and Boronizing Onabrasive Wear and Corrosion of SAE 1010, SAE 1040, D2 and 304 Steels, *Tribol. Int.*, 2003, **36**, p 155-161
7. J.H. Lee, S.H. Ahn, and J.G. Kim, Effect of Al Additions in WC-(Cr<sub>1-x</sub>Al<sub>x</sub>)N Coatings on the Corrosion Resistance of Coated AISI, D2 Steel in a Deaerated 3.5 wt.% NaCl solution, *Surf. Coat. Technol.*, 2005, **190**(2-3), p 417-427
8. J.-Q. Su, T.W. Nelson, and C.J. Sterling, Friction Stir Processing of Large-Area Bulk UFG Aluminum Alloys, *Scripta Mater.*, 2005, **52**(2), p 135-140
9. X. Du and B. Wu, Using Friction Stir Processing to Produce Ultrafine-Grained Microstructure in AZ61 Magnesium Alloy, *Trans. Nonferrous Met. Soc. China*, 2008, **18**(3), p 562-565
10. T.L. Giles, K. Oh-Ishi, A.P. Zhilyaev, S. Swaminathan, M.W. Mahoney, and T.R. McNelley, The Effect of Friction Stir Processing on the

- Microstructure and Mechanical Properties of an Aluminum Lithium Alloy, *Metall. Mater. Trans. A*, 2008, **40**(1), p 104–115
11. K. Dehghani and A. Chabok, Dependence of Zener Parameter on the Nanograins Formed During Friction Stir Processing of Interstitial Free Steels, *Mater. Sci. Eng. A*, 2011, **528**(13–14), p 4325–4330
  12. R.S. Mishra and Z.Y. Ma, Friction Stir Welding and Processing, *Mater. Sci. Eng. R*, 2005, **50**, p 1–5
  13. K. Oh-Ishikellchiro and R. McNelley, T., Microstructural Modification of As-Cast NiAl Bronze by Friction Stir Processing, *Metall. Mater. Trans.*, 2004, **35A**, p 2004–2951
  14. S.H. Aldajah, O.O. Ajayi, G.R. Fenske, and S. David, Effect of Friction Stir Processing on the Tribological Performance of High Carbon Steel, *Wear*, 2009, **267**, p 350–355
  15. Y.C. Chen and K. Nakata, Evaluation of Microstructure and Mechanical Properties in Friction Stir Processed SKD61 Tool Steel, *Mater. Charact.*, 2009, **60**(12), p 1471–1475
  16. Y. Morisada, H. Fujii, T. Mizunob, G. Abeb, T. Nagaokac, and M. Fukusomic, Nanostructured Tool Steel Fabricated by Combination of Laser Melting and Friction Stir Processing, *Mater. Sci. Eng. A*, 2009, **505**, p 157–162
  17. H. Fujii, L. Cui, N. Tsuji, M. Maeda, K. Nakata, and K. Nogi, Friction Stir Welding of Carbon Steels, *Mater. Sci. Eng. A*, 2006, **429**(1–2), p 50–57
  18. S. Wei, C. Hao, and J. Chen, Study of Friction Stir Welding of 01420 Aluminum-Lithium Alloy, *Mater. Sci. Eng. A*, 2007, **452–453**, p 170–177
  19. J. Su, T. Nelson, and C. Sterling, Microstructure Evolution During FSW/FSP of High Strength Aluminum Alloys, *Mater. Sci. Eng. A*, 2005, **405**(1–2), p 277–286
  20. P. Xue, B.L. Xiao, D. Wang, and Z.Y. Ma, Achieving High Property Friction Stir Welded Aluminium/Copper Lap Joint at Low Heat Input, *Sci. Technol. Weld. Join.*, 2011, **16**, p 657–661
  21. H.R. Zareie Rajani, A. Esmaeili, M. Mohammadi, M. Sharbati, and M.K.B. Givi, The Role of Metal-Matrix Composite Development During Friction Stir Welding of Aluminum to Brass in Weld Characteristics, *J. Mater. Eng. Perform.*, 2012, **12**, p 1–9
  22. J. Zou, T. Grosdidier, K. Zhang, and C. Dong, Mechanisms of Nanostructure and Metastable Phase Formations in the Surface Melted Layers of a HCPEB-Treated D2 Steel, *Acta Mater.*, 2006, **54**(20), p 5409–5419
  23. G.F.V. Voort, *Atlas of Time-Temperature Diagrams for Irons and Steels*, ASM International, Materials Park, 1991
  24. N. Yasavol, A. Abdollah-zadeh, M.T. Vieira, and H.R. Jafarian, Microstructure Evolution and Texture Development in a Friction Stir-Processed AISI, D2 Tool Steel, *Appl. Surf. Sci.*, 2014, **293**, p 151–159
  25. Y.S. Sato, T.W. Nelson, C.J. Sterling, R.J. Steel, and C.O. Pettersson, Microstructure and Mechanical Properties of Friction Stir Welded SAF 2507 Super Duplex Stainless Steel, *Mater. Sci. Eng. A*, 2005, **397**(1–2), p 376–384
  26. C.B. Fuller and M. Mahovey, The Effect of Friction Stir Processing on 5083-H321 5356 Al arc Welds: Microstructural and Mechanical Analysis, *Metall. Mater. Trans.*, 2006, **37A**, p 3605–33610
  27. A.H. Feng and Z.Y. Ma, Enhanced Mechanical Properties of Mg-Al-Zn Cast Alloy via Friction Stir Processing, *Scripta Mater.*, 2007, **56**, p 397–400
  28. T. Saaid, A. Abdollah-zadeh, T. Shibayanagi, K. Ikeuchi, and H. Assadi, EBSD Investigation of Friction Stir Welded Duplex Stainless Steel, *World Acad. Sci. Eng. Technol.*, 2010, **61**, p 376–379
  29. Z.Y. Ma, S.R. Sharma, and R.S. Mishra, Microstructural Modification of As-Cast Al-Si-Mg Alloy by Friction Stir Processing, *Metall. Mater. Trans.*, 2006, **37A**, p 3323–3336
  30. Z.Y. Ma, S.R. Sharma, and R.S. Mishra, Effect of Friction Stir Processing on the Microstructure of Cast A356 Aluminum, *Mater. Sci. Eng. A*, 2006, **433**(1–2), p 269–278
  31. Y. Kwon, Mechanical Properties of Fine-Grained Aluminum Alloy Produced by Friction Stir Process, *Scripta Mater.*, 2003, **49**(8), p 785–789
  32. J.-H. Huang, F.-Y. Ouyang, and G.-P. Yu, Effect of Film Thickness and Ti Interlayer on the Structure and Properties of Nanocrystalline TiN Thin Films on AISI, D2 Steel, *Surf. Coat. Technol.*, 2007, **201**(16–17), p 7043–7053